Subpolar Southern Ocean Seasonal Variability of the Geostrophic Circulation From Multi-Mission Satellite Altimetry

Matthis Auger, Jean-Baptiste Sallée, Pierre Prandi, Alberto C. Naveira Garabato

JGR Oceans

RESEARCH ARTICLE
10.1029/2021JC018096

Subpolar Southern Ocean Seasonal Variability of the Geostrophic Circulation From Multi-Mission Satellite Altimetry

Matthis Auger[1,2], Jean-Baptiste Sallée[1], Pierre Prandi[2], and Alberto C. Naveira Garabato[3]

[1]Sorbonne Université, CNRS, LOCEAN, Paris, France, [2]Collecte Localisation Satellite, Toulouse, France, [3]Ocean and Earth Science, University of Southampton, Southampton, UK

Key Points:

- A novel satellite altimetry data set is used to describe the subpolar Southern Ocean circulation seasonal cycle
- Large scale variations of surface winds are the main drivers of the Southern Ocean circulation seasonal variability
- Sea ice modulates locally the surface stress and induces an unphased seasonal mode of variability

Supporting Information:

Supporting Information may be found in the online version of this article.

Correspondence to:

M. Auger,
matthis.auger@locean.ipsl.fr

Citation:

Auger, M., Sallée, J.-B., Prandi, P., & Naveira Garabato, A. C. (2022). Subpolar Southern Ocean seasonal variability of the geostrophic circulation from multi-mission satellite altimetry. *Journal of Geophysical Research: Oceans*, *127*, e2021JC018096. https://doi.org/10.1029/2021JC018096

Received 7 OCT 2021
Accepted 29 MAY 2022

Abstract A novel multi-satellite product is used to shed light on the sea surface height seasonal cycle and associated geostrophic circulation in the subpolar Southern Ocean. We find three main modes of variability governing the Sea Level Anomaly seasonal cycle, all of them primarily governed by wind forcing. The main mode of seasonal variability is associated with the seasonality of the main subpolar gyres governed by large-scale wind stress curl, qualitatively consistent with Sverdrup dynamics. The second seasonal mode is related to the Antarctic Slope Current (ASC), governed by the coastal easterlies, with a rapid circumpolar propagation of anomalous sea-level along the continental slope that is dynamically consistent with the so-called Southern Mode. The first two modes induce an acceleration of the gyres and the ASC in winter. The third seasonal mode appears to be driven by sea ice-modulated surface stress and induces an offshore extension of the ASC from autumn to winter.

Plain Language Summary The Southern Ocean circulation has a strong impact on the global climate. Yet, the variability of the subpolar circulation features is poorly known due to the large sea ice cover, especially in winter. Here, we benefit from new satellite measurements, enabling us to measure ocean circulation in both the ice-covered and open regions of the Southern Ocean. These measurements are used to describe the seasonal cycle of the ocean circulation in the subpolar Southern Ocean, south of the Antarctic Circumpolar Current. Three processes are identified as being the main drivers of the seasonal variation of the circulation: the large scale wind variations over the whole subpolar Southern Ocean, the seasonal changes in the amplitude of the coastal winds around Antarctica, and the seasonal cycle of the sea ice, locally modifying the wind influence on the ocean surface. This study identifies the effect of these three drivers on the seasonal cycle of the subpolar Southern Ocean circulation, by highlighting their distinct seasonal variations and the regions where they are dominant.

1. Introduction

The Southern Ocean plays a central climatic role, and has provided a major service for humankind in recent decades by absorbing up to 75% of all the heat and 40% of all the carbon taken up by the world ocean, thus contributing to regulating global climate change (Frölicher et al., 2015; Meredith et al., 2019; Sallée, 2018). This key climatic role results from the four-dimensional Southern Ocean overturning circulation and associated water-mass transformations, which ventilate the deep ocean and lead to the establishment of a global ocean circulation connecting all ocean basins (Garabato et al., 2014; Talley, 2013).

The horizontal circulation of the Southern Ocean is organized around two prominent features: an eastward-flowing Antarctic Circumpolar Current (ACC) in the northern part of the Southern Ocean, and a westward-flowing Antarctic Slope Current (ASC) over the Antarctic continental slope. In between these circumpolar current systems, the subpolar Southern Ocean is spanned by large-scale regional gyres in the Weddell and Ross Seas. These subpolar gyres form the main gateway for the exchange of water masses between the global ocean and the Antarctic margins (Abernathey et al., 2016; Pellichero et al., 2017), largely set by the zonal ridges systems at their northern boundary (Wilson et al., 2022). In particular, the subpolar gyres mediate the equatorward export of the global ocean's densest water masses, formed in the Antarctic margins (Orsi et al., 1999), as well as the deep oceanic heat transport that regulates the melting of Antarctic ice shelves (Vernet et al., 2019). Despite this important role in global ocean circulation and climate, our knowledge of the circulation of the subpolar Southern Ocean remains sparse and incomplete, in part due to major observational constraints (Newman et al., 2019).

We know today that the subpolar Southern Ocean experiences a strong seasonality (Vernet et al., 2019), as suggested by a number of recent studies based on different lines of evidence. Using two moorings deployed from 1996 to 2006 in the Fimbul ice shelf region, Núñez-Riboni and Fahrbach (2009) documented the ASC's seasonal cycle and its associated forcing, and proposed a decomposition of the cycle into barotropic and baroclinic components. The ASC was found to be most intense at the end of the austral autumn, and weakest in the austral summer. Using 6 years of monthly maps of the geostrophic circulation constructed from Cryosat-2 altimetric observations in sea ice leads, Armitage et al. (2018) reached the same conclusion, but with a much wider view on the circumpolar footprint of the seasonal signal. From a similar data set, Dotto et al. (2018) presented a semi-annual intensification of the Ross Gyre in April-May and in November, while Naveira Garabato et al. (2019) showed the seasonal cycle of the geostrophic circulation over the entire subpolar Southern Ocean and linked such variations to surface winds modulated by sea ice.

In all these observational studies, wind forcing was found to be the main driver of the seasonal cycle of the ASC and subpolar gyre circulation, consistent with an analysis of numerical models (Mathiot et al., 2011). For the ASC, local wind stress was found to be the dominant forcing of the seasonal cycle, from both moorings (Núñez-Riboni & Fahrbach, 2009) and remote sensing observations (Armitage et al., 2018). However, while Armitage et al. (2018) highlighted the contribution of large-scale wind-stress curl for both Weddell and Ross gyre variability, Dotto et al. (2018) and Naveira Garabato et al. (2019) additionally emphasized the importance of taking into account the role of sea ice in modulating the wind-stress curl, to understand how changes in the subpolar Southern Ocean circulation are driven.

In this study, we complement and expand preceding descriptions of the seasonal variability of the subpolar Southern Ocean circulation by using a novel satellite altimetry product including measurements in the ice-covered regions. We use the product described in Auger et al. (2022), which is a new multi-mission Sea Level Anomaly (SLA) data set over the Southern Ocean spanning from 2013 to 2019. This product exploits recent advances in radar altimetry processing to improve measurement selection and correction. Here we analyze this 7-year high-resolution SLA product to address some of the gaps in our knowledge of the seasonal cycle of the subpolar Southern Ocean. Our aim is to unravel the multiple responses of the subpolar Southern Ocean to atmospheric forcing at seasonal time scales. In particular, our product allows us to separate the governing dynamics on and off the continental shelf (which can arguably be subject to different dynamical regimes), as well as to explore the effects of coastal winds, large-scale Sverdrup gyral circulations and sea ice, and the distinct seasonal variabilities of the on- and off-shelf sectors.

To achieve this, we apply a method based on Empirical Orthogonal Functions (EOF) decomposition to the subpolar region, allowing us to delve further into the previous analyses of the SLA seasonal cycle. This mode decomposition highlights very distinct mechanisms driving different dynamics in the region, and allows us to identify regional disparities in the geostrophic circulation links with the forcings.

2. Data and Methods

2.1. Southern Ocean SLA Product

The regional SLA product used in this paper is presented in Auger et al. (2022). It is available on SEANOE (Auger et al., 2021) with the https://doi.org/10.17882/81032. It consists of 7 years of daily SLA grids and associated geostrophic current anomalies between 2013 and 2019 on a 25 km EASE2 grid (Brodzik et al., 2012). It results from the processing and mapping of observations from three satellites: AltiKa and Sentinel-3A in the open and ice-covered oceans, and Cryosat-2 in the ice-covered regions. As described in Auger et al. (2022), the new product allows us to retrieve SLA at an increased resolution both in the open and the sea ice-covered oceans. The product also better distinguishes between on/off continental shelf regimes and exhibits fewer meridional stripes, arguably because the denser observations in the new product reduce non-physical features associated with the satellite orbit. In addition, the methodological advance reduces the risk of introducing an artificial seasonal signal phased with the sea ice that can be difficult to distinguish from physical sea-level variability (Auger et al., 2022; Prandi, 2020). The median Root Mean Square Error (RMSE) is 5.9 cm in the permanently ice-covered regions, 3.7 cm in the seasonally ice-covered ocean, and 4.0 cm in the more dynamic open ocean. Compared to similar previous products (Armitage et al., 2018; Dotto et al., 2018), the data set used here is derived using observations

from three satellites instead of only one, enabling higher spatial and temporal resolutions than before; and benefits from a novel neural network bias correction that alleviates the need for ad hoc bias correction between the open-ocean and sea ice sectors, which can introduce spurious seasonal cycle (Auger et al., 2022).

2.2. Mean Dynamic Topography

Mean geostrophic currents can be computed from the Mean Dynamic Topography (MDT), representing the mean sea surface height above the geoid. There are only a few existing MDT products. Most of the global high-resolution products do not include observations from leads, so MDTs are seasonally biased in all regions affected by sea ice cover. Therefore, to estimate the mean geostrophic currents, we choose to use Armitage et al. (2018) MDT, which has a low resolution compared to conventional open-ocean MDT products but does contain 6 years of Cryosat-2 observations in sea ice leads (Figure 1a).

We use this MDT field to define the subpolar region that we will investigate in this study, as the ocean sector south of the MDT contour −180 cm. This MDT contour is chosen as the best compromise to include the largest region possible while discarding the ACC from our analysis (Figure 1a).

2.3. Ocean Surface Stress

We investigate the effect of the momentum flux at the sea surface on the subpolar Southern Ocean SLA and dynamics. The main source of large-scale momentum flux at the ocean surface is wind stress, which we estimate from ECMWF (European Centre for Medium-Range Weather Forecasts) ERA5 monthly mean output (https://doi.org/10.24381/cds.f17050d7). The data set has a resolution of 0.25°, and is interpolated linearly on a 25 km grid. When the ocean is partially covered by sea ice, wind stress is not entirely transferred to the ocean surface, but the ocean also receives momentum through sea ice stress (Martin et al., 2016; Tsamados et al., 2014).

There remain many uncertainties in the quantification of ocean surface stress in sea ice sectors. In this paper, we use two approaches: first, we consider the wind stress, $\vec{\tau}_{ao}$, as if it was entirely transferred to the ocean surface without interference from sea ice; and second, we use an approximation of the ocean surface stress, $\vec{\tau}_{ocn}$, modulated by the presence of sea ice, which we derive from Tsamados et al. (2014) and Martin et al. (2016). Therefore, $\vec{\tau}_{ocn}$ takes into account the sea ice concentration A_i and its velocity $\vec{u}_i$ in modulating the surface stress:

$$\vec{\tau}_{ocn} = (1 - A_i)\,\vec{\tau}_{ao} + A_i \vec{\tau}_{iw}, \tag{1}$$

with:

$$\vec{\tau}_{ao} = \rho_a C_{dao} |\vec{u}_a - \vec{u}_w| \left(\vec{u}_a - \vec{u}_w\right), \tag{2}$$

and:

$$\vec{\tau}_{iw} = \rho_w C_{dw} |\vec{u}_i - \vec{u}_w| \left(\vec{u}_i - \vec{u}_w\right). \tag{3}$$

The wind stress $\vec{\tau}_{ao}$ depends on the air density $\rho_a = 1.25$ kg.m^{-3}, the air-ocean drag coefficient $C_{dao} = 1.25 \cdot 10^{-3}$ (Tsamados et al., 2014), and the wind and current velocities, respectively $\vec{u}_a$ and $\vec{u}_w$.

The sea ice concentration, A_i, is obtained through NCEI (National Centers for Environmental Information; https://doi.org/10.7265/N59P2ZTG), as well as the sea ice velocity, $\vec{u}_i$ (https://doi.org/10.5067/O57VAIT2AYYY). Both datasets are daily and have a 25 km resolution. Ocean current velocity $\vec{u}_w$ is assumed to be the geostrophic velocity and is constructed from the MDT to derive the mean velocity, to which we add an anomaly from the Auger et al. (2022) product. We use a constant ocean density of $\rho_w = 1,028$ kg.m^{-3}. We used a constant ocean-ice drag coefficient $C_{dw} = 5.50 \cdot 10^{-3}$ (Naveira Garabato et al., 2019). We also tested a variable ice drag (Lüpkes & Birnbaum, 2005; Martin et al., 2016; Tsamados et al., 2014). Both constant and variable sea ice drag coefficients showed very similar results (Figure S1 in Supporting Information S1 reproduces Figures 1b and 1c with both configurations).

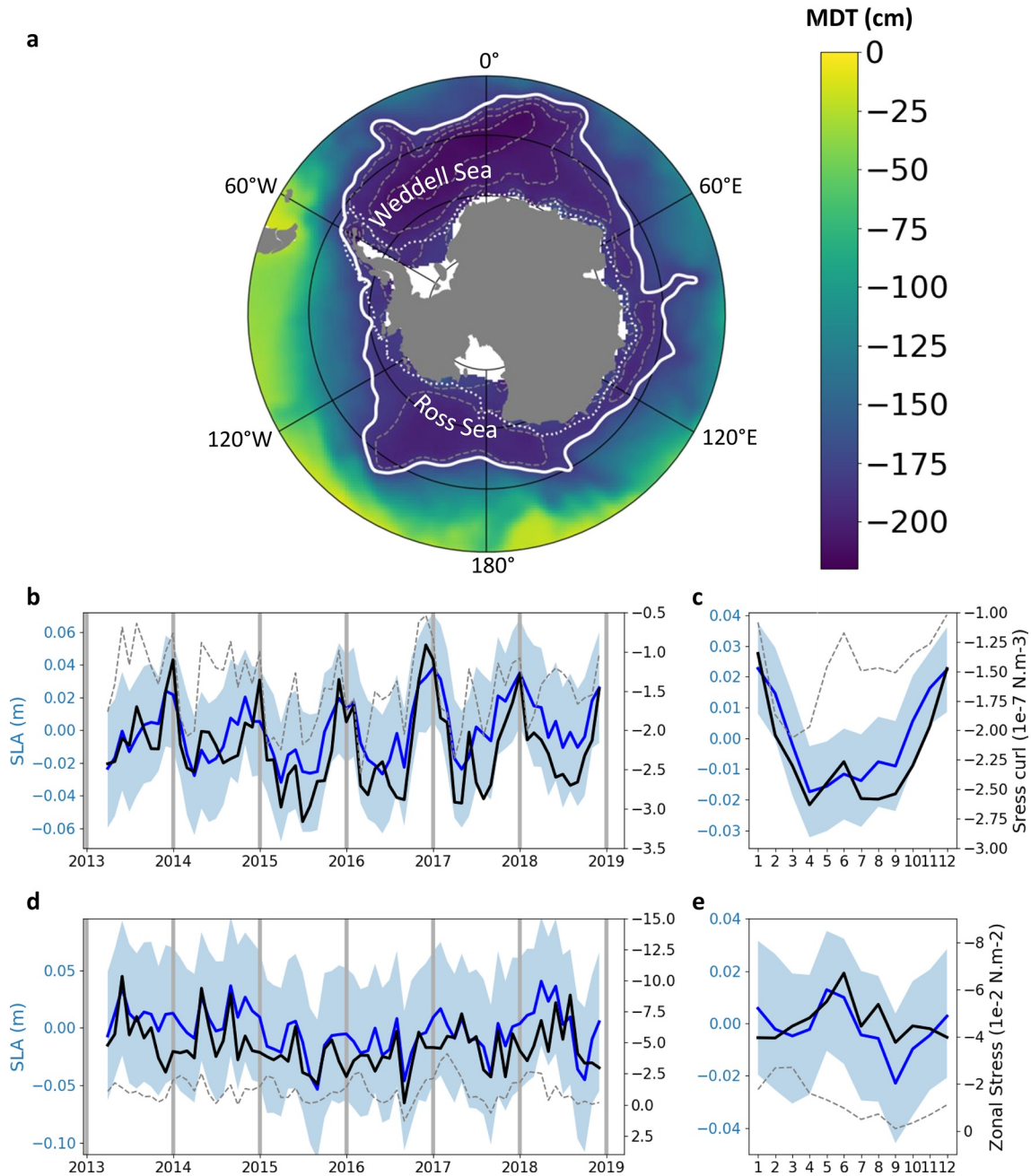

Figure 1. (a) Mean Dynamic Topography (MDT). The white line is our delimitation of the subpolar Southern Ocean, taken as the northern MDT contour at −180 cm. Black dotted lines are MDT contours of 190, 200, and 210 cm within the subpolar Southern Ocean. The white dotted line is the bathymetry contour at 1000 m and separates on-shelf and off-shelf parts of the subpolar Southern Ocean. The northern limit of the map is the 50°S latitude, and the grid shows every 10° latitude intervals from 50 to 90°S. (b) In blue, time series of the mean off-shelf monthly Sea Level Anomaly (SLA) in the subpolar Southern Ocean. Averaged Wind Stress Curl (WSC) and Ocean Stress curl in the same zone are shown in black and dashed gray, respectively. (c) Same as a, but averaged over the seasonal cycle. (d) In blue, time series of the mean on-shelf monthly SLA in the subpolar Southern Ocean. Averaged Zonal Wind Stress (ZWS) and ocean stress in the same zone are shown in black and dashed gray, respectively. (e) Same as (c), but averaged over the seasonal cycle. The blue shading shows an upper bound of the error associated with the mean SLA in each sector, derived from the seasonal maps of Root Mean Square Error between the mapped AltiKa and Cryosat-2 product and independent along-track Sentinel-3A data.

2.4. Statistical Tools

2.4.1. Correlation Significance

We use Pearson's correlation to estimate the degree of similarity between time series. Both correlation and

significance are computed based on degrees of freedom evaluated from the local temporal correlation scale presented in Auger et al. (2022), which is assumed to correspond to the time interval between two independent measurements (approximately 15 days in the subpolar Southern Ocean). Correlation significance is assessed at the 99% confidence level.

2.4.2. Robustness of the EOF Modes

The tridimensional (longitude, latitude, time) SLA signal is decomposed into Empirical Orthogonal Functions (EOFs). This entails the decomposition of the signal into several orthogonal basis functions, sorted in terms of explained variability of the signal. This decomposition here allows us to extract the main modes of variability explaining the largest percentage of variance, to then investigate each mode's forcing. We investigated the robustness of the EOF decomposition to two main sources of uncertainty: the error of the SLA product; and the choice of years analyzed in the decomposition. We present these sensitivity tests below.

Impacts of SLA product errors: The multi-mission product used in this paper comes with an estimate of the formal error from the optimal interpolation (Auger et al., 2022). It ranges from 1 to 4 cm in the subpolar Southern Ocean, and peaks at 7 cm locally in some areas of the continental shelf. To investigate the potential effect of this error on the EOF decomposition, we masked the SLA product where the formal error average was greater than 3 cm, and recomputed the EOF decomposition. The first four EOF modes, which this paper focuses on, were unaffected, with an identical value of explained variance, and associated spatial patterns and principal components (i.e., time series).

A specific region identified as potentially high-error is the permanently ice-covered area (i.e., where sea ice does not melt in summer) of the subpolar Southern Ocean, with an error ranging from 4 to 10 cm in a 2-altimeter configuration (Auger et al., 2022). As with the formal error, we computed the SLA modes while masking the permanently ice-covered region, and found that the first four EOF modes were unaffected, with the same variability explained. EOFs are also unaffected when masking both large formal error regions and permanently ice-covered parts of the subpolar Southern Ocean at the same time. We conclude from this analysis that the EOF mode decomposition presented in this paper is robust to consideration of areas with the largest SLA error.

Robustness to the choice of years included in the EOF decomposition: One of the simple methods listed by Navara & Simoncini et al., 2010 to evaluate the robustness of the modes is to apply the decomposition to subsamples of the time series. We here split the time series in two parts, and recompute the EOF analysis for each of the subsets. From April 2013 to May 2016, and from June 2016 to September 2019, the first two EOF modes recovered in each case are identical to the first two EOF modes computed with the full time series (same spatial patterns and principal components). The third mode computed from the two subsets represents, however, the fourth EOF mode computed with the full time series, with a temporal correlation of $r = 0.78$ for the first subset (2013–2016) and $r = 0.79$ for the second subset (2016–2019). This is explained by the fact that in the analysis of the full time series, the third mode primarily captures interannual variability peaking in 2016. This mode is therefore much less influential when the full time series is split into two shorter subsets. The seasonal cycle is associated with the first, second, and fourth modes of the EOF decomposition when computed over the full time series, which correspond to the first, second, and third modes of the EOF decomposition computed from the two subsets. We conclude from this analysis that the EOF mode decomposition of the seasonal cycle is robust to the choice of years analyzed.

3. Results

Large-scale SLA variability is investigated by filtering the 2013–2019 daily sea-level product with a 300 km radius Gaussian filter. The error associated with this large-scale SLA product is computed as in Auger et al. (2022) by comparing a 2-altimeter product filtered at 300 km, with the along track independent observation from Sentinel-3A data filtered with a 300 km running mean. The error is 5.7 cm in the permanently ice-covered regions, 3.0 cm in seasonally ice-covered areas, and 3.2 cm in the open ocean. The higher errors in the open ocean than in the ice-covered regions stem from the open ocean being more dynamic and therefore having a wider range of SLA values and higher SLA variability.

The choice of applying a 300 km low pass filter is motivated by wanting to focus on the larger scale variability of the subpolar Southern Ocean SLA seasonality. As a sensitivity test of the smoothing on our results, we reproduced

Table 1
Correlation Coefficient Between Averaged Sea Level Anomaly (SLA) Off-Shelf and On-Shelf, and Wind Forcing Averaged in the Same Zones

	Wind stress curl	Ocean stress curl	Zonal wind stress	Zonal ocean stress
SLA Offshelf	**0.77**	0.50	−0.58	−0.62
SLA Onshelf	0.67	0.18	**−0.70**	−0.44

Note. The bold values are the most significant correlations for investigating the mean off-shelf and on-shelf SLA. The distinction between wind stress and ocean stress curl is addressed in Section 2.3, with Equations 1–3.

the EOF decomposition presented in Section 3.3 without applying any spatial filter. The three main modes presented in that section are shown in Figures S2, S3, and S4 in Supporting Information S1. Due to smaller-scale signals that are not present in the filtered version, each unfiltered mode explains less total variance than its filtered version. However the spatial and temporal patterns are concordant between the filtered and unfiltered versions, and the main conclusions of our manuscript are insensitive to the spatial filter applied here.

We here focus on the signal in the subpolar Southern Ocean, defined as the region south of the −180 cm MDT contour to exclude the ACC from our analysis (See Method; Figure 1a). The subpolar Southern Ocean is then split into two sectors: the "off-shelf sector", north of the Antarctic continental shelf, and defined as the region to the north of the 1000 m isobath in the Antarctic continental slope; and the "Antarctic continental shelf sector", defined as the region south of the 1000 m isobath in the Antarctic continental slope (See Method; Figure 1a).

3.1. Subpolar SLA Time Series and Associated Forcing

The SLA time series averaged over the subpolar off-shelf sector shows a strong seasonal cycle, with SLA reaching a maximum in December-January and a minimum from April to October (Figures 1b and 1c). The amplitude of the seasonal cycle is ∼4 cm. Interannual variability superimposes on top of this seasonal cycle, with higher summer maxima in 2017–2018 and 2018–2019, associated both with a slightly larger amplitude of the seasonal cycle in 2017–2018, and with an underlying positive SLA trend from 2013 to 2019.

In contrast, the mean SLA averaged over the Antarctic continental shelf sector shows a strikingly different time series and seasonal cycle (Figures 1d and 1e). First, the amplitude of the seasonal cycle is much weaker than that of the interannual variability, and an important part of the seasonal cycle is in antiphase with the off-shelf seasonal cycle. The sea level on the continental shelf is maximum in early winter (May-June), and minimum in spring (September). Summer and autumn show weaker variability, with a local sea level maximum in December-January and a minimum in March. The time series also displays large interannual variability, with an amplitude of about 8 cm, more than twice as large as the amplitude of the seasonal cycle.

We now compare those time series and their seasonal cycle to the corresponding ocean surface stress, computed with $\left(\vec{\tau}_{ocn}\right)$ and without $\left(\vec{\tau}_{ao}\right)$ the influence of sea ice (respectively referred to as "ocean stress" and "wind stress"; see Methods). In both sectors, the correlation between SLA variability and wind stress variability is striking (Figures 1b–1e; Table 1). In particular, the SLA time series averaged over the off-shelf sector has a correlation of 0.77 (significant at a 99% confidence level) with the corresponding wind stress curl time series averaged over the same region (Figure 1c; Table 1). The SLA time series averaged over the continental shelf sector has an anticorrelation of 0.70 (significant at a 99% confidence level) with the zonal wind stress time series averaged over the same region (Figure 1c; Table 1). In the two sectors, the comparison between the mean SLA time series and the wind forcing shows very strong similarities, both at seasonal and interannual scales (Figures 1b and 1c). Surprisingly, when the effect of sea ice on the stress is considered (see Methods), the correlation with the SLA time series dramatically drops (Ocean Stress columns in Table 1; see also the gray dashed line in Figures 1b and 1c, which represents the time series of the Ocean Stress Curl, i.e., including the effect of sea ice on momentum transfer from the winds to the surface of the ocean). Indeed, the correlation with SLA reduces from 0.77 with the Wind Stress Curl to 0.50 with the Ocean Stress Curl. Similarly, in the on-shelf region, the correlation between the SLA and the zonal wind stress ($r = -0.70$) is higher than with the zonal ocean stress ($r = -0.44$).

Beyond the statistical correlation, there is a physical link between negative wind stress curl anomalies of the off-shelf sector and the deepening of the sea surface, through vertical Ekman pumping inducing an upwelling anomaly. Similarly, on the continental shelf, westward (i.e., negative) zonal wind stress anomalies are dynamically linked to an increase in SLA, through meridional Ekman transport anomalies.

Those two seasonal cycles show a deepening of the offshelf region and a concomitant rising of the continental shelf region in winter, and the opposite in summer. One could therefore expect an increase of the meridional gradient (cross-slope) in winter and a decrease of this gradient in summer. With a winter SLA maximum on the

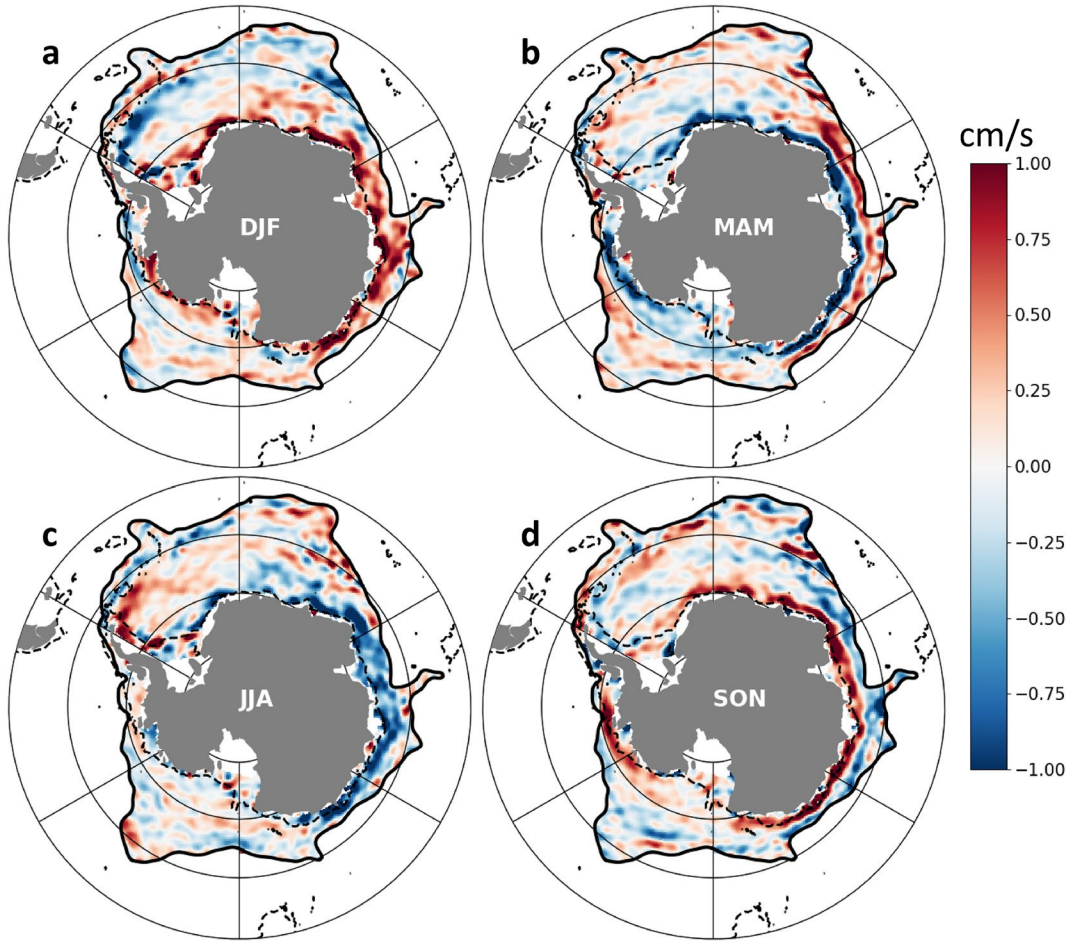

Figure 2. Zonal current anomalies of the subpolar Southern Ocean for each of the four seasons: (a) Summer (December, January, February; DJF); (b) fall (March, April, May; MAM); (c) winter (June, July, August; JJA); (d) spring (September, October, November; SON). The dotted line is the 1,000 m isobath; the black line corresponds to the northern boundary of the subpolar sector as defined in Section 2.2. Longitude and latitude limits are the same as in Figure 1a.

shelf and a minimum north of the shelf, we expect the zonal current anomaly at the slope to be westward. On the contrary, with a summer SLA minimum north of the shelf and a maximum north of the shelf, we expect the zonal current anomaly at the slope to be eastward. Therefore, we anticipate from these results that the westward ASC and southern branch of the subpolar gyres will strengthen in winter and weaken in summer.

3.2. Seasonality of Geostrophic Circulation in the Subpolar Southern Ocean

Geostrophic currents are computed from the SLA maps (Pedlosky, 2013) to investigate the seasonality of the current strength. We here focus on the seasonal cycle of the zonal geostrophic current anomaly (Figure 2). For reference, the mean zonal geostrophic current map in the subpolar Southern Ocean, showing the mean ASC and gyres circulation, is shown in Figure S5 in Supporting Information S1.

In summer (DJF), the Weddell Gyre circulation tends to weaken, as its northern branch shows a negative (westward) anomaly, while its southern branch exhibits a positive (eastward) anomaly (Figure 2a). This southern eastward anomaly actually spans almost the entire circumpolar extent of the continental shelf, indicating a circumpolar-wide summer weakening of the ASC. The winter (JJA) conditions tend to be opposite to the summer anomaly, with a winter intensification of the ASC and Weddell Gyre (Figure 2c).

The transition from summer to winter anomalies and from winter to summer anomalies at mid-season displays interesting patterns in East Antarctica, with a meridional northward spreading of the anomaly from the continental

Table 2
Sea Level Anomaly Empirical Orthogonal Functions (EOF) Modes Correlation With Their Seasonal Cycle

EOF	1	2	3	4	5	6
Correlation with its seasonal cycle	0.78	0.62	0.30	0.72	0.40	0.54
Variance explained	30%	11%	6%	5%	3%	3%

shelf to the open ocean north of the continental slope (Figures 2b and 2d). In fall (MAM), the acceleration of the ASC that continues over winter is only concentrated over the continental shelf, on the poleward edge of the current (Figure 2b), and it is only in winter that the current accelerates over its entire width. Similarly, in spring (SON), the deceleration of the ASC that continues over summer is only concentrated over the continental shelf (Figure 2d), and it is only in summer that the current decelerates over its entire width. The scale and width of the slope current are also impacted by the filtering. The resolution of the data set is 25 km. On unfiltered transects across the slope, we see zonal geostrophic current anomalies associated with the ASC on two grid points. Therefore, in that case, the ASC is 50 km wide in our data set, which may be overestimated due to the gridding of the data set. A way to have a better view of the scale of the resolved ASC jets would be to study the along-track measurements. In our case, the 300 km filtering spreads the geostrophic current anomaly to scales of 150 km, but the anomaly is still present. The inherent limitations of the data set and the filtering used may hinder the observation and the interpretations of small-scale processes that may have an impact on the subpolar Southern Ocean seasonality. Among them are the seasonal variations of the submesoscale processes under sea ice (Biddle & Swart, 2020), or of narrower variations of the ASC responding to tidal forcing, smaller-scale wind stress anomalies, and surface buoyancy forcing (Flexas et al., 2015; Stewart et al., 2019). Our focus on the large-scale signals to explore the phased variations of the SLA and geostrophic current misses the seasonality in these fine scale processes.

Figures 1b–1e show two different seasonal cycle shapes in sea surface height on the continental shelf and in the off-shelf sectors. However, those two seasonal cycles have extrema in summer and winter. They might be able to represent the summer-winter contrast in the Weddell Gyre and ASC zonal current anomalies, but they do not capture the spring and autumn offshore spreading of anomalies shown in Figure 2. To gain a deeper understanding of the mechanisms driving the seasonal cycle of geostrophic circulation in the subpolar Southern Ocean, we next apply a decomposition into Empirical Orthogonal Functions (EOFs) modes.

3.3. Spatio-Temporal Modes of Variability in the Subpolar SLA

The daily subpolar Southern Ocean SLA product is decomposed into spatial modes of variability using an EOF analysis. The first two modes stand out with respectively 30% and 11% of explained variance, while higher-order modes explain less than 6% of the total variance. As a measure of the prominence of the seasonal cycle for each mode, we compute the correlation between the time series of each mode and a synthetic time series formed as a repetition of its mean seasonal cycle (Table 2). The higher the correlation, the more prominent is the seasonal cycle compared to interannual variability for each mode. Modes 1, 2, and 4 stand out as having large seasonal cycle components. To investigate the seasonal cycle of SLA in the subpolar Southern Ocean, we will thus concentrate our analysis on these three modes.

3.3.1. A Gyre Mode

The first EOF mode of SLA (SLA_1; hereafter X_n refers to the nth mode of variable X) is associated with a prominent seasonal cycle and a spatial pattern characterized by anti-correlation between the off-shelf sector and the continental shelf sector (Figure 3a). Its principal component and in particular its seasonal cycle (Figures 3c and 3d) are reminiscent of the SLA time series averaged over the entire off-shelf sector (Figures 1b and 1c). However, the decomposition into modes of variability offers more detailed insights into the associated spatial pattern. SLA_1 is associated with a winter SLA drop that is largest at the center of the two main gyre systems in the Ross and Weddell Seas (Figure 3a), as is particularly evident for the Weddell Gyre. The spatial pattern of SLA_1 stands out as being associated with an intensification of the gyre systems in winter, with an overall eastward intensification of the geostrophic circulation at the northern edge of the subpolar sector, and a westward intensification on this sector's southern edge over the Antarctic continental slope (Figure 3b).

This mode of winter gyre intensification is strongly correlated with both the averaged wind stress curl over the off-shelf sector and the principal component of the first EOF mode of wind stress curl (respective correlation coefficients of −0.78 and 0.78, both significant at a 99% confidence level; Table 3). Figure 4 presents the first two EOF modes of the wind stress curl and the zonal wind stress, computed from a 2013–2018 time series over

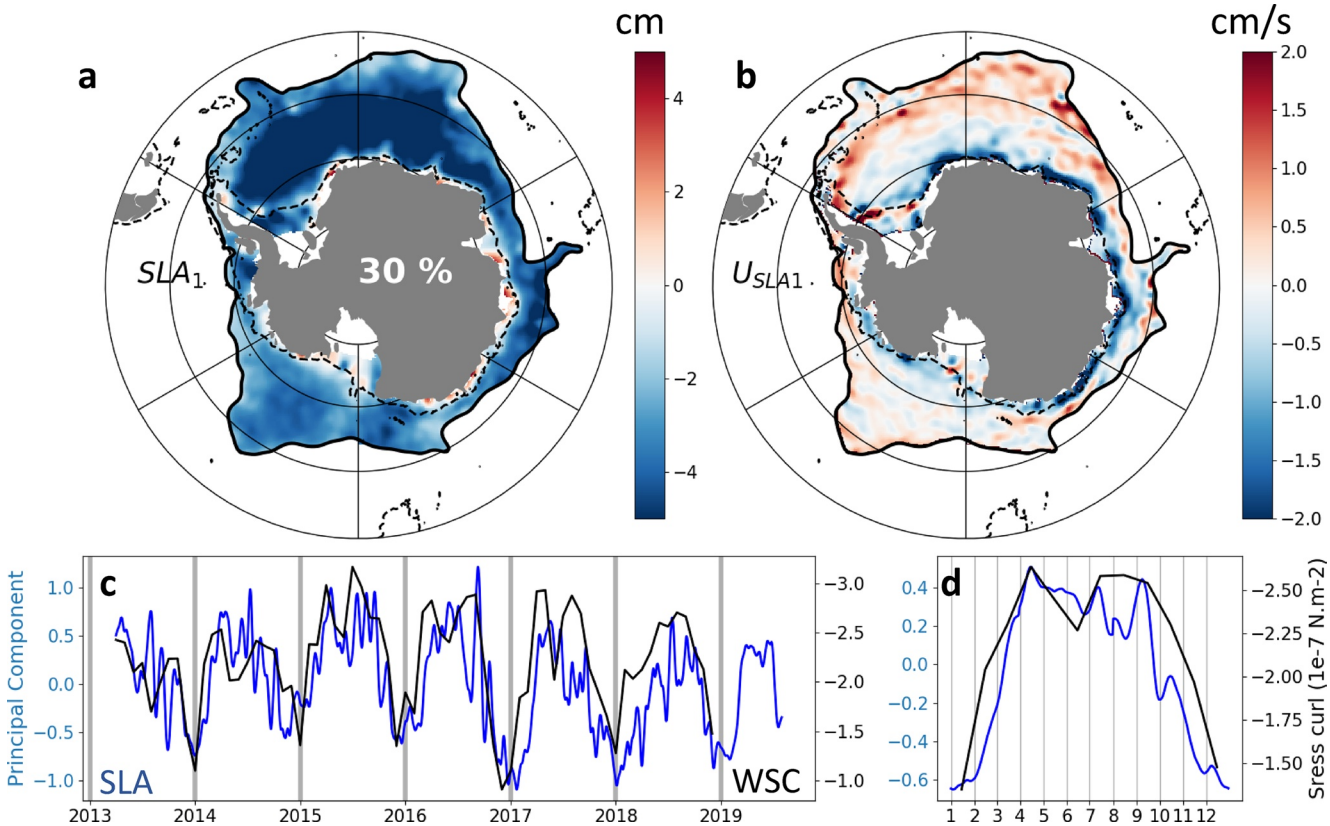

Figure 3. First Sea Level Anomaly (SLA) Empirical Orthogonal Functions (EOF) mode. (a) First Sea Level Anomaly (SLA) EOF mode spatial pattern. The dotted line is the 1000 m isobath; the black line corresponds to the northern boundary of the subpolar sector as defined in Section 2.2. The percentage is the part of total SLA variance explained by this mode. (b) Zonal geostrophic current anomaly associated with SLA mode 1. Longitude and latitude limits are the same as in Figure 1a in (a) and (b). (c) SLA Mode 1 principal component (blue), and mean wind stress curl in the off-shelf subpolar Southern ocean (black). (d) Same as (c), but for the seasonal cycle.

the subpolar Southern Ocean. It is insightful to compare the spatial pattern of the first EOF mode of SLA, SLA_1, with the spatial pattern of the first EOF mode of wind stress curl, WSC_1 (or alternatively the spatial regression of the wind stress curl onto the time series of SLA_1, see Figure S6 in Supporting Information S1). Despite the very good correlation between the time series of these two modes, the spatial patterns are distinct. SLA_1, displays a consistent pattern over the entire subpolar Southern Ocean, in contrast to WSC_1, which exhibits a meridional asymmetry. This indicates that SLA variability associated with SLA_1 does not result from a local response to local wind stress curl anomaly. Rather, SLA_1 appears to be associated with a gyre-scale response to a basin-scale anomaly of wind stress curl, as expected from classical conceptualisations of a wind-driven gyre in Sverdrup balance (Wunsch, 2011). Figure S7 in Supporting Information S1 shows this first EOF mode when decomposing to smaller sectors of the Southern Ocean. While it helps to get more details on the regional variability, the first modes of these regional decompositions are consistent with SLA_1.

Table 3
Correlation of the Time Series of the Regional Means and Principal Components of the Wind Stress Curl (WSC) and the Zonal Wind Stress (ZWS) With Sea Level Anomaly (SLA) Modes 1 and 2 Principal Components

	Offshelf		Onshelf		Mode 1		Mode 2	
	WSC	ZWS	WSC	ZWS	WSC	ZWS	WSC	ZWS
SLA mode 1	−0.78	0.58	−0.02	0.07	0.78	0.66	0.11	0.40
SLA mode 2	0.10	−0.56	−0.67	−0.72	0.20	0.45	0.49	0.66

Note. These correlations are discussed in Section 3.3 and allow to link the SLA modes with the regional wind forcing.

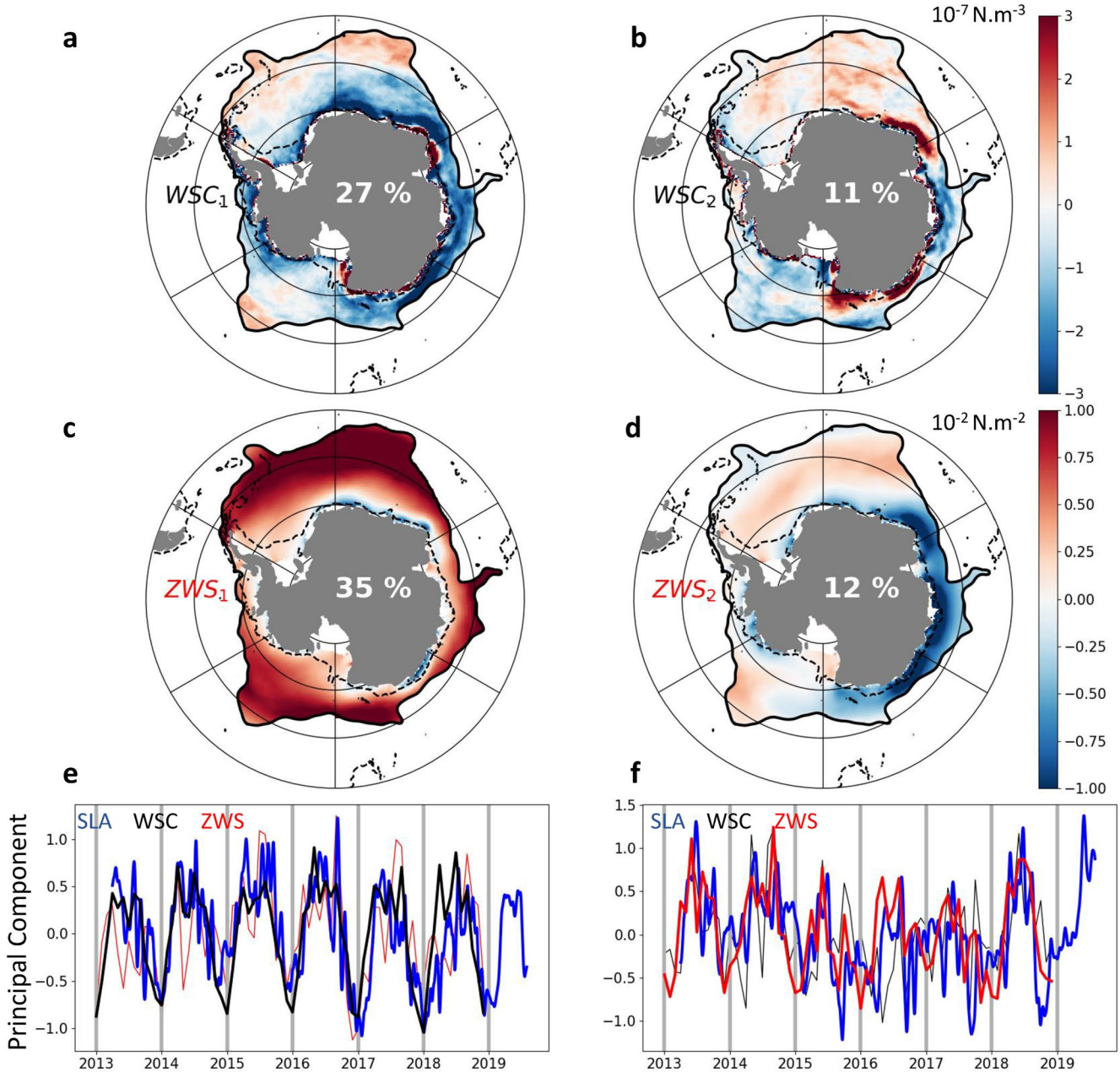

Figure 4. Wind Stress Curl (WSC) and Zonal Wind Stress (ZWS) Empirical Orthogonal Functions (EOF) modes 1 and 2 (a and b) WSC EOF modes 1 and 2 spatial patterns (c and d). ZWS EOF modes 1 and 2 spatial patterns. The percentage is the part of total variable variance explained by this mode. The dotted line on panels a–d is the 1,000 m isobath; the black line corresponds to the northern boundary of the subpolar sector as defined in Section 2.2. Longitude and latitude limits are the same as in Figure 1a in (a–d). (e) Blue, black and red lines are respectively EOF mode 1 principal components of Sea Level Anomaly (SLA), WSC, and ZWS. (f) Blue, black and red lines are respectively EOF mode 2 principal components of Sea Level Anomaly, WSC, and ZWS.

3.3.2. A Slope Current Mode

The second EOF mode of SLA, SLA_2 (Figure 5), also shows a strong seasonal cycle, though interannual variability is larger than for SLA_1. This mode displays a strong signal on the Antarctic continental shelf, with a consistent circumpolar-wide rise of sea level over the continental shelf from May to August, and a relatively invariable sea level from September to April (Figures 5a, 5c and 5d). Both the principal component and associated seasonal cycle of SLA_2 are reminiscent of the averaged SLA time series over the continental shelf (Figures 1d and 1e). The

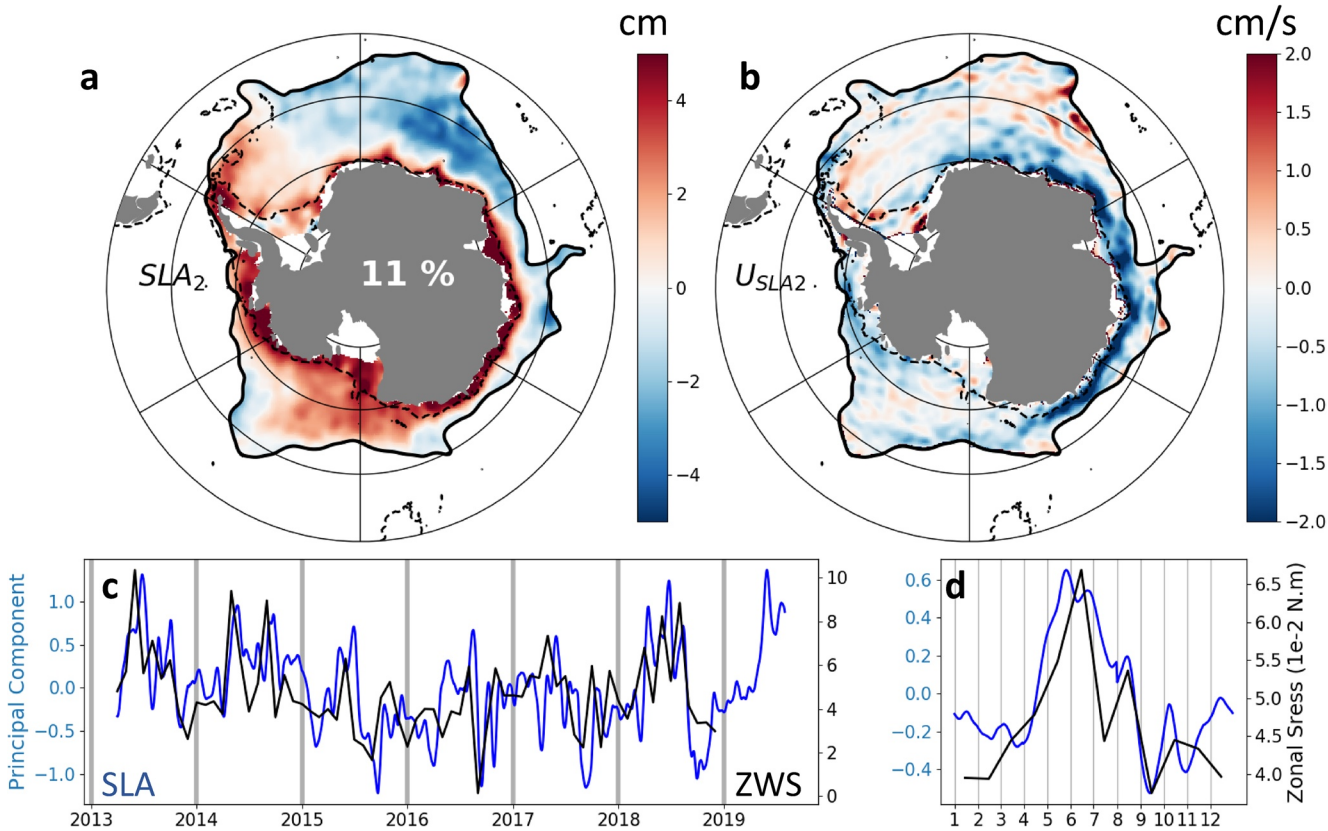

Figure 5. Second Sea Level Anomaly (SLA) Empirical Orthogonal Functions (EOF) mode. (a) Second SLA EOF mode spatial pattern. The dotted line is the 1,000 m isobath; the black line corresponds to the northern boundary of the subpolar sector as defined in Section 2.2. The percentage is the part of total SLA variance explained by this mode. (b) Zonal geostrophic current anomaly associated with SLA mode 2. Longitude and latitude limits are the same as in Figure 1a in (a and b). (c) SLA Mode 2 principal component (blue), and mean Zonal Wind Stress in the on-shelf subpolar Southern Ocean (black). (d) Same as (c), but for the seasonal cycle.

spatial pattern of SLA_2 is associated with a marked circumpolar intensification of the westward-flowing ASC in winter, represented by the strong westward zonal current anomaly at the slope in Figure 5b.

The time series of SLA_2 is highly correlated with both the time series of zonal wind stress averaged over the entire Antarctic continental shelf region and the time series of the second EOF mode of zonal wind stress (respective correlation coefficients of 0.74 and 0.64, both significant at a 99% confidence level; Table 3). Both the spatial pattern of the second EOF mode of zonal wind stress (ZWS_2) and the regression of the zonal wind stress onto the time series of SLA_2 show that the zonal wind stress pattern associated with SLA_2 is a pronounced winter intensification of the easterlies over the Antarctic continental slope (Figure 4d; Figure S6 in Supporting Information S1). However, the spatial pattern of the wind stress (Figure 4d) has a much greater degree of circumpolar asymmetry than the marked circumpolar response of SLA_2 (Figure 5a). In particular, the winter intensification of the easterlies appears confined to the East Antarctic region, while SLA_2 is associated with a winter circumpolar rise over the continental shelf. Similar to SLA_1, this mismatch of the spatial pattern concomitant with a very good correlation of the time series suggests that SLA variance associated with SLA_2 does not result from a local response to local wind stress anomaly. Instead, SLA_2 describes a circumpolar continental shelf mode, related to remote wind stress perturbations over the continental shelf, consistent with a rapid circumpolar propagation of SLA features via the so-called "Southern Mode", described from observations and numerical models (Aoki, 2002; Hughes et al., 1999, 2003). The Southern Mode is associated with coastal-trapped Kelvin waves, rapidly propagating local SLA anomalies produced by local wind forcing around the Antarctic coastline (Spence et al., 2017). The effect of the wind perturbations is strongest on the East Antarctic coastline (Figure 4d). Their effect on the Ekman transport at the coast propagates all around the continent (Figure 5a), which has a direct effect on the ASC. This response to wind perturbations can be seen in the seasonal cycle, but also projects onto this mode as interannual variability (Figure 5c). Interestingly, the SLA_2 principal component is significantly correlated $r = -0.45$ with the

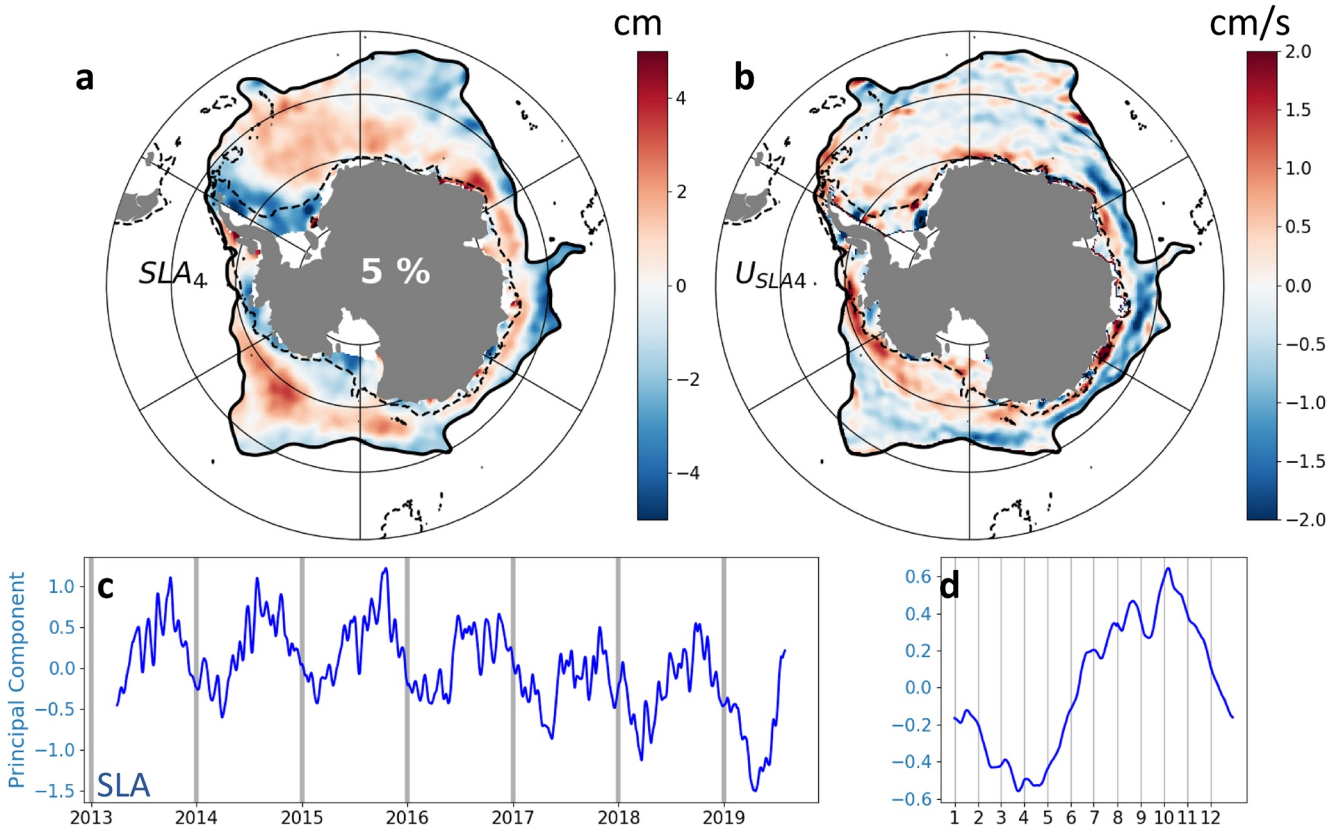

Figure 6. Fourth Sea Level Anomaly (SLA) Empirical Orthogonal Functions (EOF) mode. (a) Fourth SLA EOF mode spatial pattern. The dotted line is the 1,000 m isobath; the black line corresponds to the northern boundary of the subpolar sector as defined in Section 2.2. The percentage is the part of total SLA variance explained by this mode. (b) Zonal geostrophic current anomaly associated with SLA mode 4. (c) SLA Mode 4 principal component. Longitude and latitude limits are the same as in Figure 1a in (a and b). (d) Same as (c), but for the seasonal cycle.

Southern Annular Mode. Figure S8 in Supporting Information S1 shows this first EOF mode when decomposing to smaller sectors of the Southern Ocean. While it helps to get more details on the regional variability, the first modes of these regional decompositions are consistent with SLA_2.

Therefore, while the first mode could be described as a subpolar gyre mode, the second can be described as an ASC mode. Although the spatial patterns of the two first EOF modes of SLA are different, the two modes consistently describe a winter intensification of the subpolar ocean circulation (Figures 2a–2d). However, none of these two modes capture the mid-season current anomaly described in Figures 2a–2d. In order to better grasp the potential drivers of such mid-season anomalies, we next investigate higher EOF modes of variability. In particular, we focus on the next mode that has a strong imprint of seasonal signal, the fourth EOF mode of SLA, SLA_4 (See Table 2). The third SLA mode is not discussed here, as it shows no strong seasonal cycle but only interannual variability (Table 2). It is however displayed in Figure S9 in Supporting Information S1, and shows opposite variations in the Ross and Weddell seas sectors, peaking in early 2013 and mid-2016.

3.3.3. Unphased Mode - Modulation by Sea Ice

SLA_4 shows a large seasonal cycle that is not phased with the seasonal cycles of SLA_1 and SLA_2 (Figure 6). While SLA_1 and SLA_2 are associated with an acceleration of the large-scale current systems in the winter months, SLA_4 is instead linked to a circumpolar westward intensification of currents over the continental shelf at the end of summer and before winter, between February and May, which then slows down with a maximum deceleration at the beginning of winter (Figures 6b and 6d). This continental shelf signal is accompanied by an opposite anomaly of the geostrophic circulation to the north of the continental slope.

This mode, while explaining only 5% of the total variance, stands out as important for the mid-season anomalies. Indeed, modes 1 and 2 alone do not explain the full seasonality of the zonal currents. Figure S10 in Supporting

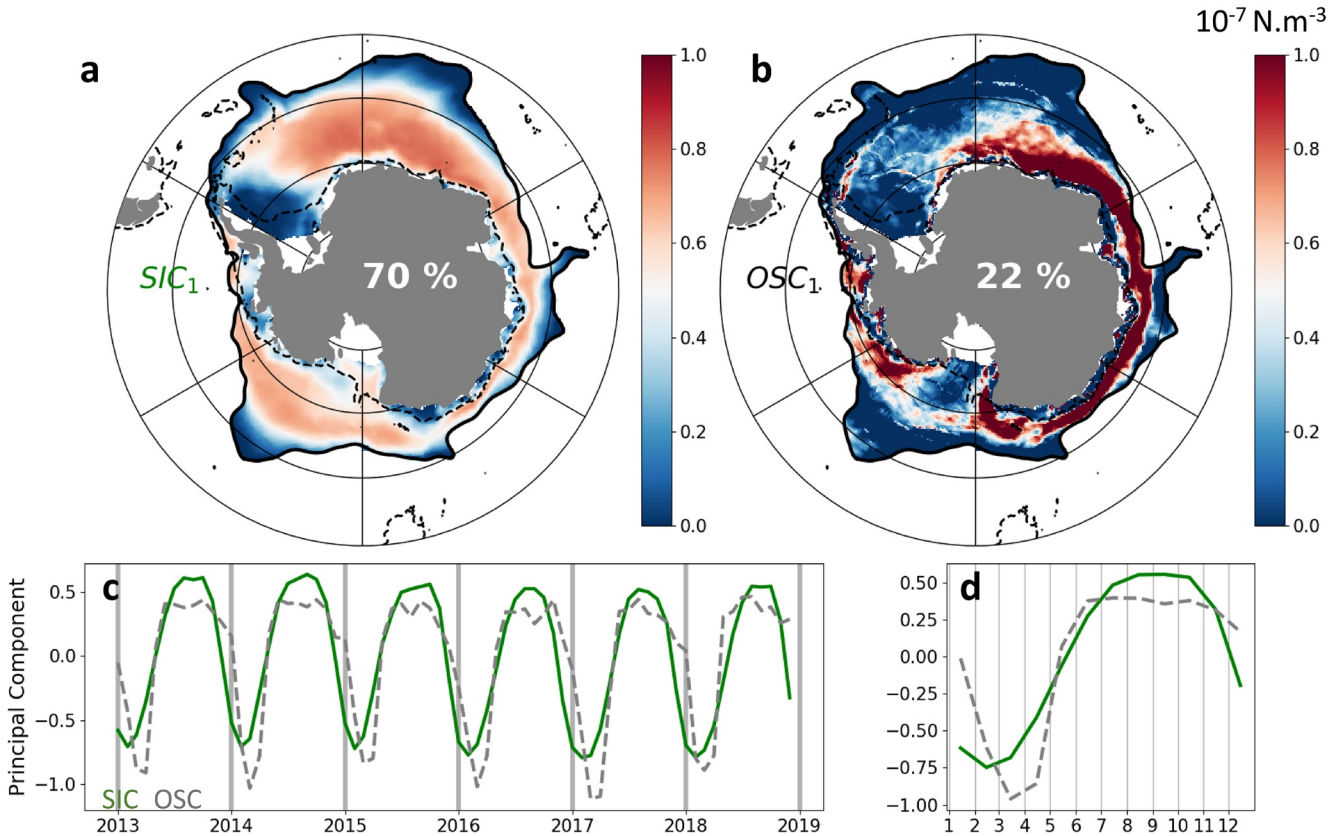

Figure 7. Sea Ice concentration (SIC) and Ocean Stress curl (OSC) first Empirical Orthogonal Functions (EOF) modes. (a) Sea ice concentration (SIC) EOF mode 1 spatial pattern. Colorbar boundaries are not centered on 0 for a better comparison with Figure 6a. The dotted line is the 1000 m isobath; the black line corresponds to the northern boundary of the subpolar sector as defined in Section 2.2. (b) OSC EOF mode 1 spatial pattern. Longitude and latitude limits are the same as in Figure 1a in (a and b). (c) In green, SIC mode 1 principal component. In dashed green, OSC mode 1 principal component. (d) Seasonal cycles of both principal components.

Information S1 shows the reconstructed seasonality of the zonal geostrophic current anomalies from only modes 1 and 2. The reconstructed seasonality is different from the seasonality of the full signal (Figure 2). In particular, they miss the MAM and SON zonally banded structure occurring at the continental slope in Figure 2. Figure S11 in Supporting Information S1 shows the reconstructed seasonality of the zonal geostrophic current anomalies from modes 1, 2, and 4. It is only when considering mode 4 that this mid-season banded structure is properly explained. Therefore, while Mode 4 is associated with relatively low variance, because it is associated with a spatial pattern mostly confined to a small region near the continental slope, this mode is of importance to explain the mid-season variability of the slope current. We also note that the difference of explained variance between modes 1 and 2 and mode 4 is much reduced when performing EOF analysis on SLA maps on which we do not apply a 300-km filter.

SLA_4 highlights the northward spreading of the ASC anomalies, from Autumn to Winter (Figure 2bc), and from Spring to Summer (Figure 2ad). This kind of northward migration of the jet is possible in the case of a background potential vorticity (PV) gradient associated with bathymetric features, such as the Antarctic continental slope (Peña-Molino et al., 2016; Stern et al., 2015). However, SLA_4 is highly seasonal, and is very consistent with the main mode of variability of sea ice concentration (Figures 7a, 7c and 7d), both in terms of the time series (correlated at 0.74, significant at the 99% confidence level) and of the spatial pattern (Figures 7a and 6a). This striking relationship suggests that sea ice might have a role in shaping SLA_4. Sea ice can have a thermodynamical effect through steric expansion, but this would have an opposite impact to the one observed, as winter brine rejection contracts the upper-ocean water column. Alternatively, sea ice can have a mechanical effect by modulating momentum transfer at the sea surface. Interestingly, the first EOF mode of the ocean stress curl (see Methods) is well correlated with SLA_4 both in terms of the time series ($r = 0.72$, significant at a 99% confidence level) and the spatial pattern (Figures 7b and 6a). In autumn, the sea ice cover is small, and along-slope easterlies induce

on-shelf Ekman transport. The divergence between easterlies and westerlies induces negative SLA anomalies just north of the slope. In winter and spring, sea ice extent reaches hundreds of kilometers north of the continental slope. At the ice edge, the interaction of winds with the marginal ice zone may create upwellings or downwellings impacting the local dynamics (Häkkinen, 1986). Here, the sea ice cover tends to reduce the wind stress that reaches the ocean surface between the slope and the sea ice edge. Figure S12 in Supporting Information S1 shows the mean ratio between the wind stress $|\vec{\tau}_{ao}|$ and the ice stress $|\vec{\tau}_{iw}|$ for the October months. In the marginal ice zone, $|\vec{\tau}_{ao}|$ is greater than twice $|\vec{\tau}_{iw}|$ for 77% of the gridpoints. There, the decay of the wind stress applied to the ocean due to the sea ice cover dominates the surface stress meridional gradient. In consequence, the sea ice cover will create a strong momentum stress in the MIZ. More precisely, winter-spring intensified westerlies are still strong north of the ice edge (See ZWS_2, Figure 4d), inducing southward Ekman transport and convergence between the slope and the sea ice edge, while divergence is displaced northward. This combination of wind and sea ice seasonal cycles results in a zonally banded structure of SLA seasonal variations, leading to two strong SLA gradients at the slope and the sea ice edge and thereby creating two jets with opposite directions at the scale resolvable by our 300-km filter (Figure 6b). While such modulation of local wind stress curl by the presence of sea ice appears as a compelling explanation for this mode of variability, we are not able to exclude other potential explanations such as a delayed adjustment of isopycnals at the gyre boundaries in response to seasonally varying wind stress curl at the gyre scale (Meneghello et al., 2018; Su et al., 2014).

Overall, this mode leads to a northward spreading of ASC acceleration from summer to winter and deceleration from winter to summer. This northward spreading of the acceleration is consistent with the mooring observations of (Núñez-Riboni & Fahrbach, 2009) at longitude 0°, which revealed an off-shelf westward maximum in June, 1 month after the strongest westward maximum was reached earlier over the slope.

4. Conclusion and Discussion

A novel satellite-based SLA product fitted to recover SLA in sea ice-covered regions is used to investigate the seasonal cycle of subpolar Southern Ocean geostrophic currents. The seasonal cycle of SLA in the subpolar Southern Ocean is primarily explained by three main modes of variability. The first mode corresponds to a winter acceleration of the Weddell and Ross gyres, consistent with large-scale variability of wind stress curl, through Sverdrup dynamics. The second mode is associated with a winter intensification of the ASC, forced by easterly wind variability on the continental shelf, with a circumpolarly propagating signal consistent with the so-called Southern Mode (Hughes et al., 2003). The third mode is a mid-season northward progression of the ASC acceleration/deceleration that is consistent with a local response to surface stress modulated by the combination of sea ice and wind stress seasonal cycles.

Our results are in line with those of Armitage et al. (2018), who linked the integrated wind stress curl with the geostrophic ocean circulation in the Ross and Weddell gyres. We however propose that in addition to the wind stress at large scales, which drives the two main modes of seasonal ocean circulation variability, a complete description of the seasonal cycle requires consideration of the local effects of sea ice modulating the stress received by the ocean. This is consistent with Naveira Garabato et al. (2019), who highlighted the important role of sea ice in modulating the momentum stress received by the ocean. In addition, our results allow us to delineate on-shelf and off-shelf dynamics, and to highlight their distinct seasonal cycles, owing to the use of a multi-satellite product to recover SLA variability at higher spatio-temporal resolution than previously achievable.

Using moorings, Núñez-Riboni and Fahrbach (2009) described a delay of several months between on-shelf and off-shelf ASC maxima. Over the 9 years they analyzed, they found that the ASC's barotropic component reaches a maximum in April on the continental shelf, while the ASC maximum was only reached 2 months later directly to the north of the continental slope. This was explained by the northward displacement of the ice edge in winter seasonally moving the maximum of momentum transfer. Our ice-related mode and zonal current climatology (Figures 2 and 6) are consistent with this result, and provide an overarching vision of this process all around Antarctica. In East Antarctica and in the Amundsen-Bellingshausen seas, where the seasonal variation of sea ice extent is weak, the ASC's response to sea ice modulation of the surface stress is stronger, as the sea ice edge moves northward but stays in regions of strong westerlies. The impact on the ASC is lower in the Weddell and Ross Gyres as the sea ice expands northward, for the sea ice edge is displaced too far from the slope to have a strong impact on the ASC.

Both Flexas et al. (2015) and Stewart et al. (2019) discussed the important effect of the tides and eddies in maintaining the Antarctic Slope Front and forcing the ASC. These processes were not considered in this study, as SLA was filtered prior to analysis and large scale seasonal variations of the circulation were consistent with atmospheric-driven processes. However, the Auger et al. (2022) high resolution product may have the potential for observing some mesoscale features in the subpolar Southern Ocean, including in its ice-covered parts. This could be a perspective for future research. More generally, future sea surface height products merging even more satellite observations, or new instruments allowing observations of sea surface topography at higher resolution (e.g., the NASA/CNES mission SWOT [Biancamaria et al., 2016]), provide promising avenues to investigate smaller-scale processes in sea ice regions, although it remains unclear how it will perform in those regions.

Our results allow us to identify the forcing of the main features of the subpolar Southern Ocean current system. While the gyres appear tied to large-scale wind stress curl, the slope current responds more to the coastal easterlies. In a context of changing climate, Southern Hemisphere westerlies are projected to intensify (except for aggressive mitigation scenarios), and the seasonality of coastal easterlies is expected to increase (Hazel & Stewart, 2019). We can therefore anticipate that while Southern Ocean subpolar gyres are being and will likely continue to be spun up in response to increasing westerlies, the ASC will mostly accelerate in winter, while it may slow down in summer in response to weaker easterlies. While future changes in sea ice cover are still unclear, as sea ice changes regionally or circumpolarly, the mid-season transitions of the Antarctic Slope Current seasonal cycle are likely to be affected by local surface stress modulation.

Data Availability Statement

The Sea Level Anomaly data used in this study are available at Auger et al. (2021) via the https://doi.org/10.17882/81032 and described in Auger et al. (2022).

Acknowledgments
M.A. and J.-B.S. have received funding from the European Union's Horizon 2020 research and innovation program under grant agreement N821001. M.A. was funded through a CNES/CLS scholarship.

References

Abernathey, R. P., Cerovecki, I., Holland, P. R., Newsom, E., Mazloff, M., & Talley, L. D. (2016). Water-mass transformation by sea ice in the upper branch of the Southern Ocean overturning. *Nature Geoscience*, *9*(8), 596–601. https://doi.org/10.1038/ngeo2749

Aoki, S. (2002). Coherent sea level response to the Antarctic Oscillation. *Geophysical Research Letters*, *29*(20), 11–14. https://doi.org/10.1029/2002GL015733

Armitage, T. W. K., Kwok, R., Thompson, A. F., & Cunningham, G. (2018). Dynamic topography and sea level anomalies of the Southern ocean: Variability and teleconnections. *Journal of Geophysical Research: Oceans*, *123*(1), 613–630. https://doi.org/10.1002/2017JC013534

Auger, M., Prandi, P., & Sallée, J.-B. (2021). Daily Southern ocean sea level anomaly and geostrophic currents from multimission altimetry, 2013–2019. *SEANOE*. https://doi.org/10.17882/81032

Auger, M., Prandi, P., & Sallée, J.-B. (2022). Southern ocean sea level anomaly in the sea ice-covered sector from multimission satellite observations. *Scientific Data*, *9*(1), 70. https://doi.org/10.1038/s41597-022-01166-z

Biancamaria, S., Lettenmaier, D. P., & Pavelsky, T. M. (2016). The SWOT mission and its capabilities for land hydrology. *Surveys in Geophysics*, *37*(2), 307–337. https://doi.org/10.1007/s10712-015-9346-y

Biddle, L. C., & Swart, S. (2020). The observed seasonal cycle of submesoscale processes in the Antarctic marginal ice zone. *Journal of Geophysical Research: Oceans*, *125*(6), e2019JC015587. https://doi.org/10.1029/2019JC015587

Brodzik, M. J., Billingsley, B., Haran, T., Raup, B., & Savoie, M. H. (2012). EASE-grid 2.0: Incremental but significant improvements for Earth-gridded data sets. *ISPRS International Journal of Geo-Information*, *1*(1), 32–45. https://doi.org/10.3390/ijgi1010032

Dotto, T. S., Naveira Garabato, A., Bacon, S., Tsamados, M., Holland, P. R., Hooley, J., et al. (2018). Variability of the Ross gyre, Southern ocean: Drivers and responses revealed by satellite altimetry. *Geophysical Research Letters*, *45*(12), 6195–6204. https://doi.org/10.1029/2018GL078607

Flexas, M. M., Schodlok, M. P., Padman, L., Menemenlis, D., & Orsi, A. H. (2015). Role of tides on the formation of the Antarctic slope Front at the Weddell-Scotia confluence. *Journal of Geophysical Research: Oceans*, *120*(5), 3658–3680. https://doi.org/10.1002/2014JC010372

Frölicher, T. L., Sarmiento, J. L., Paynter, D. J., Dunne, J. P., Krasting, J. P., & Winton, M. (2015). Dominance of the Southern ocean in Anthropogenic carbon and heat uptake in CMIP5 models. *Journal of Climate*, *28*(2), 862–886. https://doi.org/10.1175/JCLI-D-14-00117.1

Garabato, N., Williams, A. C., Williams, A. P., & Bacon, S. (2014). The three-dimensional overturning circulation of the Southern Ocean during the WOCE era. *Progress in Oceanography*, *120*, 41–78. https://doi.org/10.1016/j.pocean.2013.07.018

Häkkinen, S. (1986). Coupled ice-ocean dynamics in the marginal ice zones: Upwelling/downwelling and eddy generation. *Journal of Geophysical Research*, *91*(C1), 819–832. https://doi.org/10.1029/JC091iC01p00819

Hazel, J. E., & Stewart, A. L. (2019). Are the near-Antarctic easterly winds weakening in response to Enhancement of the southern Annular mode? *Journal of Climate*, *32*(6), 1895–1918. https://doi.org/10.1175/JCLI-D-18-0402.1

Hughes, C. W., Meredith, M. P., & Heywood, K. J. (1999). Wind-driven transport fluctuations through drake passage: A southern mode. *Journal of Physical Oceanography*, *29*(8), 1971–1992. https://doi.org/10.1175/1520-0485(1999)029

Hughes, C. W., Woodworth, P. L., Meredith, M. P., Stepanov, V., Whitworth, T., & Pyne, A. R. (2003). Coherence of Antarctic sea levels, southern Hemisphere Annular mode, and flow through drake passage. *Geophysical Research Letters*, *30*(9). https://doi.org/10.1029/2003GL017240

Lüpkes, C., & Birnbaum, G. (2005). "Surface drag in the Arctic marginal sea-ice zone: A comparison of different parameterisation concepts". *Boundary-Layer Meteorology*, *117*(2), 179–211. https://doi.org/10.1007/s10546-005-1445-8

Martin, T., Tsamados, M., Schroeder, D., & Feltham, D. L. (2016). The impact of variable sea ice roughness on changes in Arctic Ocean surface stress: A model study. *Journal of Geophysical Research: Oceans*, *121*(3), 1931–1952. https://doi.org/10.1002/2015JC011186

Mathiot, P., Goosse, H., Fichefet, T., Barnier, B., & Gallée, H. (2011). Modelling the seasonal variability of the Antarctic slope current. *Ocean Science*, *7*(4), 455–470. https://doi.org/10.5194/os-7-455-2011

Meneghello, G., Marshall, J., Campin, J.-M., Doddridge, E., & Timmermans, M.-L. (2018). The ice-ocean governor: Ice-ocean stress feedback limits Beaufort gyre Spin-up. *Geophysical Research Letters*, *45*. https://doi.org/10.1029/2018GL080171

Meredith, M., Sommerkorn, M., Cassotta, S., Derksen, C., Ekaykin, A., & Hollowed, A. (2019). Polar regions. In *IPCC special report on the ocean and cryosphere in a changing climate*.

Navarra, A., & Simoncini, V. A. (2010). *Guide to Empirical Orthogonal Functions for Climate Data Analysis*. Springer Science & Business Media. https://doi.org/10.1007/978-90-481-3702-2

Naveira Garabato, A. C., Dotto, T. S., Hooley, J., Bacon, S., Tsamados, M., Ridout, A., et al. (2019). Phased response of the subpolar Southern Ocean to changes in circumpolar winds. *Geophysical Research Letters*, *46*(11), 6024–6033. https://doi.org/10.1029/2019GL082850

Newman, L., Heil, P., Trebilco, R., Katsumata, K., Constable, A., van Wijk, E., et al. (2019). Delivering Sustained, coordinated, and integrated observations of the Southern ocean for global impact. *Frontiers in marine Science*, *6*. https://doi.org/10.3389/fmars.2019.00433

Núñez-Riboni, I., & Fahrbach, E. (2009). Seasonal variability of the Antarctic coastal current and its driving mechanisms in the Weddell Sea. *Deep-Sea Research I*, *56*(11), 1927–1941. https://doi.org/10.1016/j.dsr.2009.06.005

Orsi, A. H., Johnson, G. C., & Bullister, J. L. (1999). Circulation, mixing, and production of Antarctic bottom water. *Progress in Oceanography*, *43*(1), 55–109. https://doi.org/10.1016/S0079-6611(99)00004-X

Peña-Molino, B., McCartney, M. S., & Rintoul, S. R. (2016). Direct observations of the Antarctic slope current transport at 113°E. *Journal of Geophysical Research: Oceans*, *121*(10), 7390–7407. https://doi.org/10.1002/2015JC011594

Pedlosky, J. (2013). Geophysical fluid dynamics. *Springer Science & Business Media*.

Pellichero, V., Sallée, J.-B., Schmidtko, S., Roquet, F., & Charrassin, J.-B. (2017). The ocean mixed layer under Southern Ocean sea-ice: Seasonal cycle and forcing. *Journal of Geophysical Research: Oceans*, *122*(2), 1608–1633. https://doi.org/10.1002/2016JC011970

Prandi, P. (2020). Multi-mission sea level in the Arctic Ocean. (Tech. Rep. No. CLS-ENV-NT-20-0126). *CLS*.

Sallée, J.-B. (2018). Southern ocean warming. *Oceanography*, *31*(2). https://doi.org/10.5670/oceanog.2018.215

Spence, P., Holmes, R. M., Hogg, A. M., Griffies, S. M., Stewart, K. D., & England, M. H. (2017). Localized rapid warming of West Antarctic subsurface waters by remote winds. *Nature Climate Change*, *7*(8), 595–603. https://doi.org/10.1038/nclimate3335

Stern, A., Nadeau, L.-P., & Holland, D. (2015). Instability and mixing of zonal jets along an idealized continental shelf break. *Journal of Physical Oceanography*, *45*(9), 2315–2338. https://doi.org/10.1175/JPO-D-14-0213.1

Stewart, A. L., Klocker, A., & Menemenlis, D. (2019). Acceleration and overturning of the Antarctic slope current by winds, eddies, and tides. *Journal of Physical Oceanography*, *49*(8), 2043–2074. https://doi.org/10.1175/JPO-D-18-0221.1

Su, Z., Stewart, A. L., & Thompson, A. F. (2014). An idealized model of Weddell gyre export variability. *Journal of Physical Oceanography*, *44*(6), 1671–1688. https://doi.org/10.1175/JPO-D-13-0263.1

Talley, L. D. (2013). Closure of the global overturning circulation through the Indian, Pacific, and Southern Oceans: Schematics and transports. *Oceanography*, *26*.

Tsamados, M., Feltham, D. L., Schroeder, D., Flocco, D., Farrell, S. L., Kurtz, N., et al. (2014). Impact of variable atmospheric and oceanic form drag on Simulations of Arctic Sea Ice. *Journal of Physical Oceanography*, *44*(5), 1329–1353. https://doi.org/10.1175/JPO-D-13-0215.1

Vernet, M., Geibert, W., Hoppema, M., Brown, P. J., Haas, C., Hellmer, H. H., et al. (2019). The Weddell Gyre, Southern Ocean: Present knowledge and future challenges. *Reviews of Geophysics*, *57*(3), 623–708. https://doi.org/10.1029/2018RG000604

Wilson, E. A., Thompson, A. F., Stewart, A. L., & Sun, S. (2022). Bathymetric control of subpolar gyres and the overturning circulation in the Southern ocean. *Journal of Physical Oceanography*, *52*(2), 205–223. https://doi.org/10.1175/JPO-D-21-0136.1

Wunsch, C. (2011). The decadal mean ocean circulation and Sverdrup balance. *Journal of Marine Research*, *69*. https://doi.org/10.1357/002224011798765303